Journal of Engineering Research 13 (2025) 1924–1935

Contents lists available at ScienceDirect

Journal of Engineering Research

journal homepage: www.journals.elsevier.com/journal-of-engineering-research

# Sensitivity of the endwall flow in a linear vane cascade to blade fillet geometry

Adeola S. Shote [a,b,*], Gazi I. Mahmood [a,c]

[a] Department of Mechanical and Aeronautical Engineering, University of Pretoria, South Africa
[b] Department of Mechanical Engineering, Olabisi Onabanjo University, Ago Iwoye, Nigeria
[c] Department of Mechanical Engineering, Prince Mohammad Bin Fahd University, Al Khobar 31952, Saudi Arabia

ARTICLE INFO

*Keywords:*
Endwall
Fillet
Passage vortex
Axial vorticity
Pressure loss
Pitchwise pressure

ABSTRACT

Based on the blade chord and inlet velocity, the current computational study uses a linear vane cascade with a large filleted blade-endwall junction with a 2.01 x $10^5$ Reynolds number. Three fillets with related profiles are explored. To evaluate the upshots of geometric differences in a fillet attached to the endwall flow-field, the height and endwall-width of the fillets are changed. The RANS k-ω turbulent model is used in the computations, and the results are compared to experimental results from a similar cascade without the fillet. The computed results of the secondary flow-field in the endwall region along the cascade are compared for baseline (no fillet) and filleted passages. As a result of diminished leading-edge and passage vortices, the fillets lower pitchwise pressure gradients, flow separation, axial vorticity, and overall pressure losses when compared to the baseline. The pros of fillets on endwall secondary flows are however unaffected by fillet's geometric changes.

## Introduction

A major source of aerodynamic diminutions in turbine blade path ways is attributed to the secondary flows near the endwall boundary. The secondary flows form at the leading-edge of blade-endwall junction then advect heat in the passage along the endwall as the three-dimensional vortical structures. These vortical flows also decrease the film cooling penetration on the endwall and increase the neighborhood heat transfer emanating from the hot-gas to the passage walls. Investigations [1–3] in the vane- and rotor-blade cascades show modifications of the blade-endwall junction and endwall profile employing fillets and two- or three-dimensional contour reduce the vigour, size and effects of the endwall secondary flows. The present numerical study investigates the effects of fillet profile at the vane-endwall junction on the near endwall flow-field and secondary flow losses in a linear cascade. The fillet geometric parameters are changed to show their influences on the reduction of the secondary flows in the passage.

The evolution and structures of the pressure and suction side-leg vortices around the leading edge and along the endwall of vane cascades have been studied before by Kang & Thole [4] and Hermanson *et al.* [5]. The creation of the passage vortex is due to the boundary layer and cross flow generated by pitchwise pressure gradients at the endwall region [6]. Numerical and experimental studies by Saha & Acharya [7], Torre [8] present the control of endwall region vortices by profiling the cascade linear-endwall. The results of [7,8] show that endwall flow losses and heat transfer can be significantly reduced. Ligrani *et al.* [9] describe the various study models of secondary flows and ways for managing them in blade cascades.

In [6,7,10–19], the effects of large fillets at the blade leading-edge and linear-endwall junction on cascade secondary flows, loss coefficients, flow angles, and pitchwise pressure gradients were investigated. For the investigations, the blade geometry in the stationary cascade is either a rotor- or vane-blade profile of a gas turbine engine. The findings of [3,4,7–16] show that the leading-edge fillet alters the locations and structures of secondary flows, resulting in decreased endwall heat transfer and aerodynamic losses in cascade passage. The alterations are largely induced upstream of the throat region by the fillet. The amount of decrease in aerodynamic losses, such as turbulent kinetic (TK) energy and total pressure dissipation, is determined by the fillet surface profile and shape. Shih and Lin [12] cascade inlet conditions with the leading-edge fillet greatly reduce overall pressure losses, but Saha *et al.* [17] cascade exit conditions increase pressure losses. Becz *et al.* [11,13] observations compare total pressure losses owing to secondary flows using leading-edge bulbs and parabolic fillets. According to the findings of [11,13], losses reduce with fillets but rise with bulbs. Unlike the findings of [6,7,10–19], the findings of [2,20] reveal that the tiny fillet at the blade-endwall junctions all around increases secondary

* Corresponding author at: Department of Mechanical and Aeronautical Engineering, University of Pretoria, South Africa.
*E-mail address:* u14145295@tuks.co.za (A.S. Shote).

https://doi.org/10.1016/j.jer.2024.06.009
Received 3 February 2024; Received in revised form 27 May 2024; Accepted 16 June 2024
Available online 25 June 2024

**Nomenclature**

| | |
|---|---|
| $C$, $C_{ax}$ | blade true chord and axial chord |
| $C_{p,blade}$ | coefficient of pressure on blade |
| $C_{pt,loss}$ | total pressure loss coefficient |
| $C_{p,static}$ | static pressure coefficient on endwall |
| $P$ | blade pitch |
| $P_{b,x}$, $P_{e,x}$ | blade pressure, pressure on endwall |
| $P_{t,r}$, $P_{s,r}$ | total pressure, static pressure at reference |
| $P_{t,x}$ | local total pressure |
| $PS$, $SS$ | pressure side, suction side |
| Re | Reynolds number |
| $S$ | blade span |
| $LE$, $TE$ | blade leading-edge, trailing-edge |
| $U$ | freestream velocity along '$X$' |
| $X$, $Y$, $Z$ | local coordinates |
| $X_G$, $Y_G$, $Z_G$ | global coordinates |
| $Yaw_{local}$ | local yaw angle of flow |
| $m_{in}$ | mass flow rate in a blade passage |
| $s$ | blade surface distance from leading edge |

*Greek*

| | |
|---|---|
| $\Delta$ | change in quantities related |
| $\omega$ | vorticity |
| $\rho$, $\mu$ | air density and viscosity |

*Subscripts*

| | |
|---|---|
| b,x | local blade quantity related to '$X$' |
| e,x | local endwall quantity |
| mass-av | mass-averaged quantity |
| s,r | static quantity related to reference plane |
| t,r | total quantity related to reference plane |
| t,x | local total quantity related to '$X$' direction |

losses in the blade passageways. In addition, the improved fillet of [21] has a negligible effect on the annular vane cascade's exit secondary flows.

While the benefits of leading-edge fillets in terms of aerodynamic loss reductions are known from prior studies, the sensitivity of the loss reductions to changes in the geometric characteristics of a specific fillet has not been thoroughly investigated. Due to production tolerances and precision, the fillet geometric dimensions may fluctuate and thus could positively or negatively affect the turbulence, flow separation and could creating additional pressure loss penalties near the endwall region. Study of the effect of the alteration in fillet geometry could have tremendous running cost and noise implications. These computational studies will afford access for the exploration of larger data set without increase in time and resources. Besides, visual data and results will be made easier compared to experimentation which previously creates inaccessibility of critical data due to their complexity. This is an urgent gap that this investigation is trying to bridge effectively at the shortest possible time. The research also attempts to present integration of data from multiple sources, including experimental data. Therefore, the need for this investigation is imperative to give detailed insight for turbine innovators and manufacturers. The effects of fillet height and breadth variations on the endwall region flow field in a cascade model are reported in this computational study. A low-speed linear cascade test facility with a vane-blade profile is simulated using the cascade model. From the leading-edge to the throat area within the tunnel, the big fillet at the vane-endwall junction is used in the current cascade. The experimental scenario validates the numerical model for the baseline situation without a fillet. Between the baseline and fillet examples, details of the endwall flow field are examined, including streamlines, vorticities, pressure distributions, and total pressure diminutions through the passage. As a result, the findings of this study are critical in the development of high-efficiency turbine endwalls.

## Measurements and experimental setup

The computational model is validated using data collected from an experimental cascade facility. The airstream wind tunnel, which contains the cascade (linear in arrangement) test section, is depicted schematically in Fig. 1(a). The air get is produced by the suction of dual duct fans with a combined capacity of 22.5 kW linked in series configuration at the exit of the tunnel, which functions in an open circuit. The tunnel has a rectangular cross-section with wood-paneled walls. Clear polycarbonate serves as the test section's walls. Through a honey-comb screen and a passive turbulence grid, ambient air is allowed to accelerate gradually and flow progressively into the test section. Seven two-dimensional vane-blades are housed in the test section area of the cascade facility, as illustrated in Fig. 1(a). In addition, the blade geometry is constructed by extruding (24 cm) the first stage (GE-E$^3$) nozzle guide vane's hub-side blade profile [22]. At the engine hub, the cascade geometry is 6 times that of the actual nozzle geometry. The vanes are made of polycarbonate. They have a flat surface that is coated with polyurethane. The specifications used in the cascade test segment geometry are listed in Table 1. At the engine's vane leading-edge, the approaching flow angle is fixed to zero degrees. To produce the periodic flow condition in the test section, some airflow upstream of the tunnel section is diverted via the sidewalls of blade 1 and blade 7. The flow assessments are carried out in the opaque zone between blade 3 and blade 5 in Fig. 1(a). Surface pressures may be measured using pressure tap holes located in the mid-span positions of blades 3, 4, and 5.

A slot on the apex side of the endwall at 2.5 $C_{ax}$ upstream of the cascade intake, as illustrated in Fig. 1(a), permits the pitot-static probe and hot-wire anemometer to monitor the reference parameters in Table 2. Table 2 shows the freestream celerity $U$ measured from the endwall, above the boundary layer. The density value in Table 2 is presumed constant in the observations due to the little pressure drop over the test cascade. As illustrated in Fig. 1(b), the Reynolds number in the table is calculated using the freestream velocity emanating from the reference plane, actual chord length of the vane. At atmospheric temperature, the viscosity of air is determined. Fig. 1(b) also shows the coordinate systems and computational model. The global coordinates ($X_G$, $Y_G$, $Z_G$) start at the blade-3's leading edge. The pressure side of the blade 3 is where the local coordinates (X, Y, Z) emanate. After that, the position ($Z_G$ or $Z = 0$) corresponds to a location on the endwall. On the pressure side, the blade-profile coordinate (denoted as 's') in Fig. 1(b) begins at the leading-edge which is positive. For the computational flow analysis and measurements, Fig. 1(b) also illustrates the axial, $X_G/C_{ax}$ positions of the pitchwise Plane-1 and −2 in the cascade channel. Part of the passage throat area is included in Plane-1. Plane-2 is a little further downstream from the passage's outlet.

The endwall pressure distributions are measured using a series of pressure taps on the top endwall between blades 3 and 4. To scan the flow-field, a five-hole total-pressure probe with a tip diameter of 1.6 mm is used through the endwall slot at Plane-2. Separate differential pressure transducers are attached to each of the wall-static pressure taps and pressure-probe ports. The pressure signals are sent by the transducers to a National Instruments™ data collecting system. The signals from each transducer are then recorded for 2 seconds at a frequency of 100 Hz by a LabVIEW™ software controlling the probe traverse. After applying the proper calibrations, the voltage responses are time-averaged and transformed to the pressure. The average uncertainties in the velocity

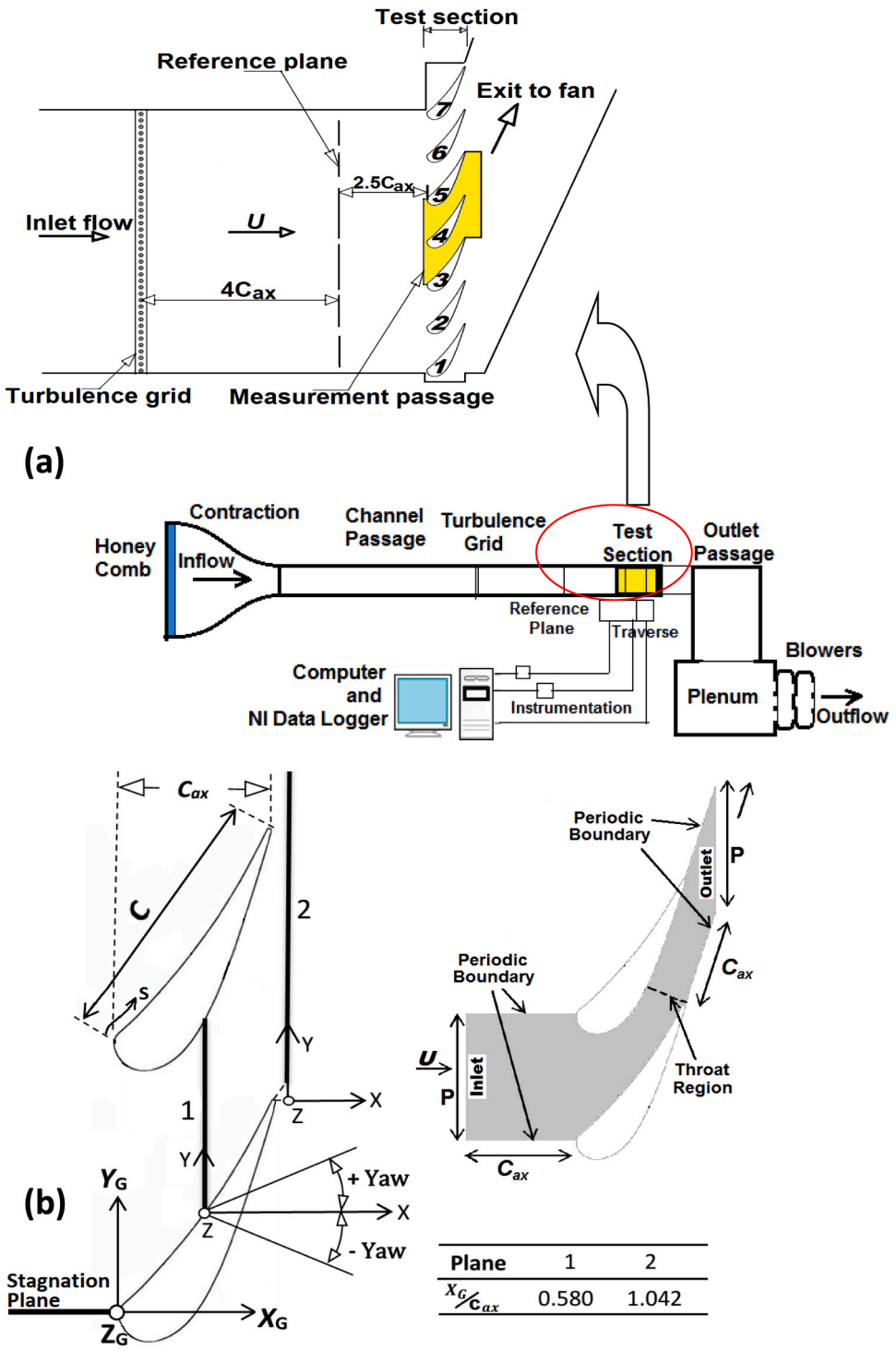


| Plane | 1 | 2 |
|---|---|---|
| $X_G/C_{ax}$ | 0.580 | 1.042 |

**Fig. 1.** Schematic representations of: (a) cascade test setup, and (b) flow-analysis planes (measurement and computations), coordinates systems, and computational domain without the fillet.

**Table 1**
Geometric specifications of blade cascade.

| $C_{ax}$ (m) | C (m) | C/S | C/P | Incidence |
|---|---|---|---|---|
| 0.2031 | 0.3551 | 1.4791 | 1.3281 | 0° |

and pressure data, based on the 95 % confidence level [23], are 6.0 % and 5.0 %, respectively.

### Fillet design and geometry

At the blade-endwall intersection, the computational model uses three fillet designs. Fig. 2 depicts the geometry of the fillets (Fillet-1, −2, and −3). On the two sides (pressure and suction), the endwall fillet profiles perfectly match the curve of the blade profile, as seen in the figure. On both sides of the blade profile, the fillets cover the leading-

**Table 2**
Reference flow variables at 2.5Cax upstream of test cascade inlet.

| | Experiment | Computations |
|---|---|---|
| Freestream velocity, $U$ (m/s) | 10.0 | 10.0 |
| $P_{s,r}$ (kPa), absolute | 88 | 101.9 |
| Boundary layer thickness | 0.10 S | 0.10 S |
| Streamwise turbulence intensity | 2.0 % | 2.0 % |
| Air temperature (K) | 298 | 300 |
| Air density, ρ (kg/m$^3$) | 1.021 | 1.021 |
| Reynolds Number, Re =ρUC/μ) | 2.01E+05 | 2.01E+05 |

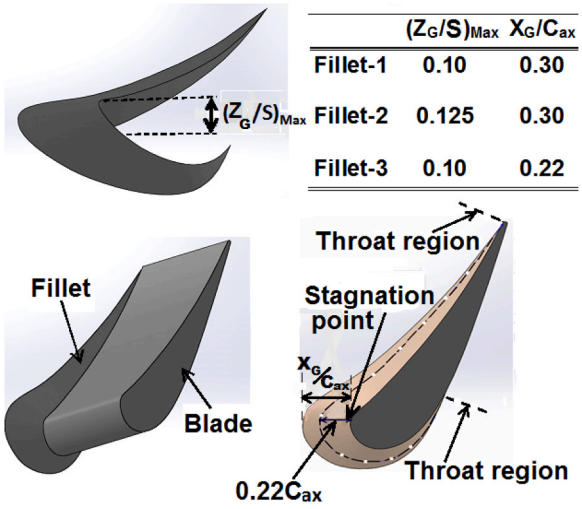


**Fig. 2.** Fillet profile geometries.

edge area and continue to the throat point in the passage. On the pressure and suction sides of the blade, the passage throat is positioned between $X_G/C_{ax} \approx 1.0$ and 0.6, respectively. As shown in Fig. 2, the blade trailing-edge area is part of the throat. On both the pressure and suction sides, the surface height of all the fillets varies linearly from the blade surface to the endwall, as well as from the leading-edge to the throat. At the throat, the fillet profiles meld nicely with the blade-wall and endwall at the same time. The differences between the three fillets are determined by variations in the endwall's maximum height and breadth, as shown in the table in Fig. 2. The measurements taken in the cascade facility are taken without the use of a fillet.

## Model of the computation

The computational model utilizes the blade passage with periodic boundary conditions as shown in Fig. 1(b) and as described in Table 1 to recreate the precise cascade geometry used in the experiment. The model's intake and exit flow boundaries are 2.5 $C_{ax}$ upstream and 1.0 $C_{ax}$ downstream of the blade leading and trailing edges, respectively. At the inlet and outlet boundaries, the inlet velocity with the user-defined boundary layer profile and the pressure outlet boundary conditions are employed. The computational inlet velocity profile is created using the obtained velocity data in the experimental reference plane. The input for the flow domain is air as the working fluid as characterized in Table 2. The adiabatic walls such as the blade surface and endwall are specified for the solid boundaries of Fig. 1(b).

To discretize the computational domain and solve for the conservation of mass and momentum equations, the commercial STAR-CCM+™ [24] is utilized. In the STAR-CCM+™, the k-$\omega$ turbulent model is used in the Reynolds Averaged Navier-Stokes (RANS) equations. Because the pressure differential between the inlet and outlet boundaries in the experimental cascade is low, the incompressible flow solver is used at steady-state. In the discretization of the computational domain, the STAR-CCM$^{+TM}$ polyhedral unstructured meshes are used. A 15-prism-layer refined mesh is used to resolve the boundary layers on the walls. The domain extends up to the mid-span region ($Z_G/S = 0.5$) along the span ($Z_G$ direction), where the symmetry wall boundary is applied to decrease the number of computational cells and time. To produce a $y+ < 1$ at the solid walls, the total number of computational cells is approximately $1.6 \times 10^{+6}$. Iterations are performed until the normalized residuals for the solutions of the continuity, momentum, turbulent kinetic energy, and shear-stress dissipation rate equations are resolved below $10^{-4}$. When the adiabatic fillets are added in Fig. 1(b), the computational domain and volume discretization remain the same as indicated.

## Discussions of results

### *Experimentation*

The experimental results are obtained without the fillet (baseline) in the cascade and presented to validate results from the computational model without the fillets. The test data are measured with the periodic flow conditions in the blade passages. The periodic flow conditions are achieved when the pressure distributions on the blade surfaces are equal at the corresponding locations [25]. The flow periodicity in the experimental cascade is thus ensured by matching the pressure distributions on the blades 3, 4, and 5 at the spanwise locations of $Z_G/S = 0.5$. The baseline manifestation in the results presented always refers to experimental or computational results without the fillet.

### *Transport equations*

The governing equations employed by the STAR-CCM+™ [24] for the finite volume discretization are the incompressible Navier-Stokes equations in the continuous integral form as in Eq. (1). The definitions and the details of the symbols related to this equation henceforth are provided in [24] and are not provided here for brevity. Eq. (2) is the discrete form of the Navier-Stokes equations for the cell- centered control volume.

$$\underbrace{\frac{d}{dt}\int_V \rho\chi\varphi \; dV}_{\substack{\text{transient}\\ \text{term}}} + \underbrace{\oint_A \rho\varphi(v - v_g) \; . \; da}_{\substack{\text{convective}\\ \text{flux}}} = \underbrace{\oint_A \Gamma\nabla\varphi \; . \; da}_{\substack{\text{diffusive}\\ \text{flux}}} + \underbrace{\int_V S_\varphi \; dV}_{\substack{\text{volumetric source}\\ \text{term}}} \tag{1}$$

$$\frac{d}{dt}(\rho\chi\varphi \; V)_0 + \sum_f [\rho\varphi \; (v \; . \; a \; - \; G)]_f = \sum_f (\Gamma \; \nabla\varphi \; . \; a \;)_f + (S_\varphi \; V)_0 \tag{2}$$

In the equations above, $G,\varphi,\chi,\ S,v_g,\Gamma,a,\nabla,V,t$, and $v$ denote the grid flux, scalar quantity, porosity, vector between cell face and centroid, grid velocity, diffusivity, area vector, gradient operator, volume, time, and velocity, respectively. The total number of equations corresponds to the total number of cells in the grid volume. The second order gradient flux $G_f$ is given by Eq. (3) with $\delta V_j^n$ as the swept volume for each cell face. The second order transient term is dropped out due to the steady-state. Eqs. (4) - (8) provide the second-order upwind scheme of discretization of the convective term. The terms $(\nabla\varphi)_{r,0}$ and $(\nabla\varphi)_{r,1}$ are the gradients in cell 0 and 1.

$$G_f = \frac{\left(3\,\delta V_j^n \; - \; \delta V_j^{n-1}\right)}{2\,\Delta t} \tag{3}$$

$$[\rho \; \varphi \; (v{\cdot}a - G)]_f = \begin{cases} \dot{m}_f^{\varphi} f,0 \;\; for \; \dot{m}_f \geq 0 \\ \dot{m}_f^{\varphi} f,1 \;\; for \; \dot{m}_f < 0 \end{cases} \tag{4}$$

$$\varphi_{f,0} \;\; = \;\; \varphi_0 \;\; + \;\; s_0 \; . \; (\nabla\varphi)_{r,0} \tag{5}$$

$$\varphi_{f,1} \;\; = \;\; \varphi_0 \;\; + \;\; s_1 \; . \; (\nabla\varphi)_{r,1} \tag{6}$$

$$s_0 = x_f - x_0 \quad (7)$$

$$s_1 = x_f - x_1 \quad (8)$$

*Grid sensitivity*

Grid independence of the solutions is tested with different number of volume cells in the baseline model without the fillet. The outcomes are compared in Fig. 3(a) for the mass-averaged total pressure loss coefficients, $(C_{pt,loss})_{mass\text{-}av}$ from Eq. (9) at different pitchwise-planes along the blade passage. The losses in Fig. 3(a) differ by only 2 % or less in each plane as the cell number changes.

$$(C_{pt,loss})_{mass-av} = \frac{1}{m_{in}} \int \left[\frac{P_{t,r} - P_{t,x}}{0.5\rho\, U^2}\right] (\rho\, u_x)\, dA \quad (9)$$

*Validation of computational model*

Experimental and computational results of the static pressure coefficient, $C_{p,blade}$ distributions at midspan locations ($Z_G/S = 0.5$) on the blade profile ($s/C$) are compared in Fig. 3(b). The coefficient, $C_{p,blade}$ is computed from Eq. (10) where $P_{b,x}$ is the local pressure on the blade profile. The computational results for the Fillet-1 are also included in the figure.

$$C_{p,blade} = \frac{(P_{b,x} - P_{s,r})}{0.5\rho\, U^2} \quad (10)$$

In Fig. 3, the blade's stagnation region is at s/C = 0.0, where $C_{p,blade}$ is the maximum (b). On both the pressure side (PS) and the suction side (SS), the flow accelerates on the blade surface away from the stagnation zone, lowering the surface pressures, $P_{b,x} < P_{s,r}$, and $C_{p,blade}$. The lowest surface pressure in the channel throat area is shown by a drop in $C_{p,blade}$ distributions on the suction side (SS) at s/C ≈ −0.26 in Fig. 3(b). $C_{p,blade}$ values peak at $s/C < -0.26$ on the suction side when the flow slows downstream of the throat area (SS). The numerical calculations successfully anticipate the observed $C_{p,blade}$ between $-0.25 < s/C < 0.70$, according to the comparisons in Fig. 3(b). On the pressure and suction sides (i.e. $s/C < -0.25$ and $s/C > 0.75$), the experimental $C_{p,blade}$ values deviated somewhat from the numerical values as they got closer to the trailing edge. The slight disparity is most likely due to (i) the numerical model's inaccuracy in predicting the point of a transition from laminar to turbulent boundary layer on the blade, and [26] the ambiguity in the exact locations of measurements on the blade. The Fillet-1 $C_{p,blade}$ distribution is quite similar to the numerical baseline scenario, indicating that blade loading at the mid-span is unchanged.

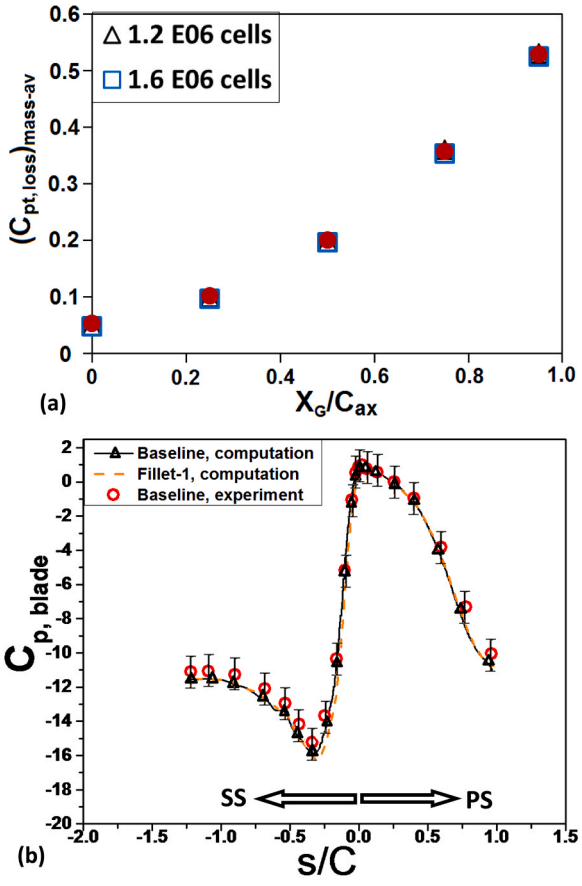


**Fig. 3.** (a) Grid sensitivity of mass-averaged coefficients, $(C_{pt,loss})_{mass\text{-}av}$ along blade passage without fillet, and (b) $C_{p,blade}$ along blade profile at mid-span ($Z_G/S = 0.5$) location.

$$C_{p,static} = \frac{(P_{s,r} - P_{e,x})}{0.5\rho\, U^2} \quad (11)$$

The total pressure loss coefficient, $C_{pt,\,loss}$ distributions in plane-2 for the baseline scenarios are compared in Fig. 4 between the experiment and the simulations. The loss coefficients, $C_{pt,loss}$, are calculated from $P_{t,x}$ in the plane using Eq. (12). The normalized local pitchwise and spanwise locations are indicated by the axes (Y/P, Z/S) in Fig. 4. The pressure losses in the passage-vortex core in Plane-2 are depicted by the high contour values of total pressure loss coefficient in the area between 0.3 < Y/P < 0.9 and Z/S < 0.2 in Fig. 4. The interaction between the trailing-edge wake and passage-vortex outer area is depicted by the greater $C_{pt,loss}$ region at Y/P ≥ 0.9. These elevated contour values of the total pressure loss coefficient are prominently observed in the spatial region where the normalized distance along the Y/P ranges between 0.3 and 0.9, and the normalized distance along the Z/S is less than 0.2. This delineates the impact of the trailing-edge wake on the passage-vortex outer area, emphasizing the dynamic flow phenomena in this specific region.

Additionally, the interaction between the wake trailing-edge and the outer region of the passage vortex is highlighted by a distinct area of higher total pressure loss coefficient ($C_{pt,loss}$) values. Investigation of [8, 20] also has passage vortex core structures that are similar to this research. The contour values from the computations in the passage-vortex core area slightly differ from those from the experiment when compared with the data in Fig. 4. The computations, on the other hand, reasonably describe the size and position of the passage-vortex core from when compared with that of the experiment.

$$C_{pt,loss} = \frac{(P_{t,r} - P_{t,x})}{0.5\rho U^2} \quad (12)$$

*Endwall pressure coefficient, $C_{p,static}$ (computations)*

Fig. 5 shows the coefficient distributions, $C_{p,static}$, obtained from the $P_{e,x}$ and Eq. (11) computational results along the endwall for the three fillets. The blade and fillet positions are indicated in the image by the light and dark colored zones, respectively. $C_{p,static}$ values grow along the endwall as the flow accelerates, as shown in Figs. 5(a) - 5(d), and are maximum (between $C_{p,static} = 10$ and 13) near the route throat area. The contour values change minimally between the baseline and fillet scenarios when the $C_{p,static}$ distributions are compared in Fig. 5(a) and Figs. 5(b) - 5(d) for the computations.

The high streamline turnings in the pitch direction in the boundary layer are caused by pitchwise pressure gradients on the endwall, which enhance the passage vortex [7,8]. The differences in local pressure coefficients on the endwall, $C_{p,static}$, are presented along the axial direction, $X_G/C_{ax}$, in Fig. 6 to examine the impacts of the fillets on the pitchwise pressure differential at endwall with clarity. The endwall $C_{p,\,static}$ difference between the pressure side (PS) and suction side (SS) of

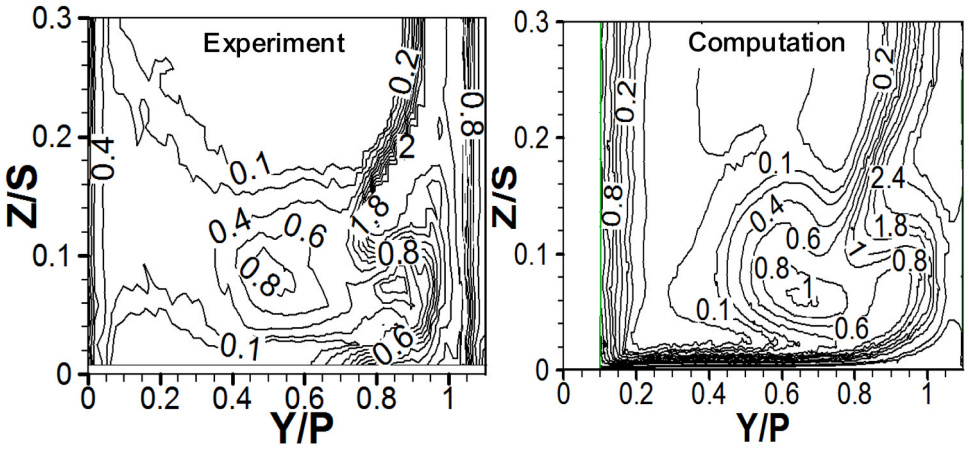


**Fig. 4.** Comparisons of baseline pressure coefficients between experiment and computations: $C_{pt,loss}$ in Plane-2 at $X_G/C_{ax} = 1.04$.

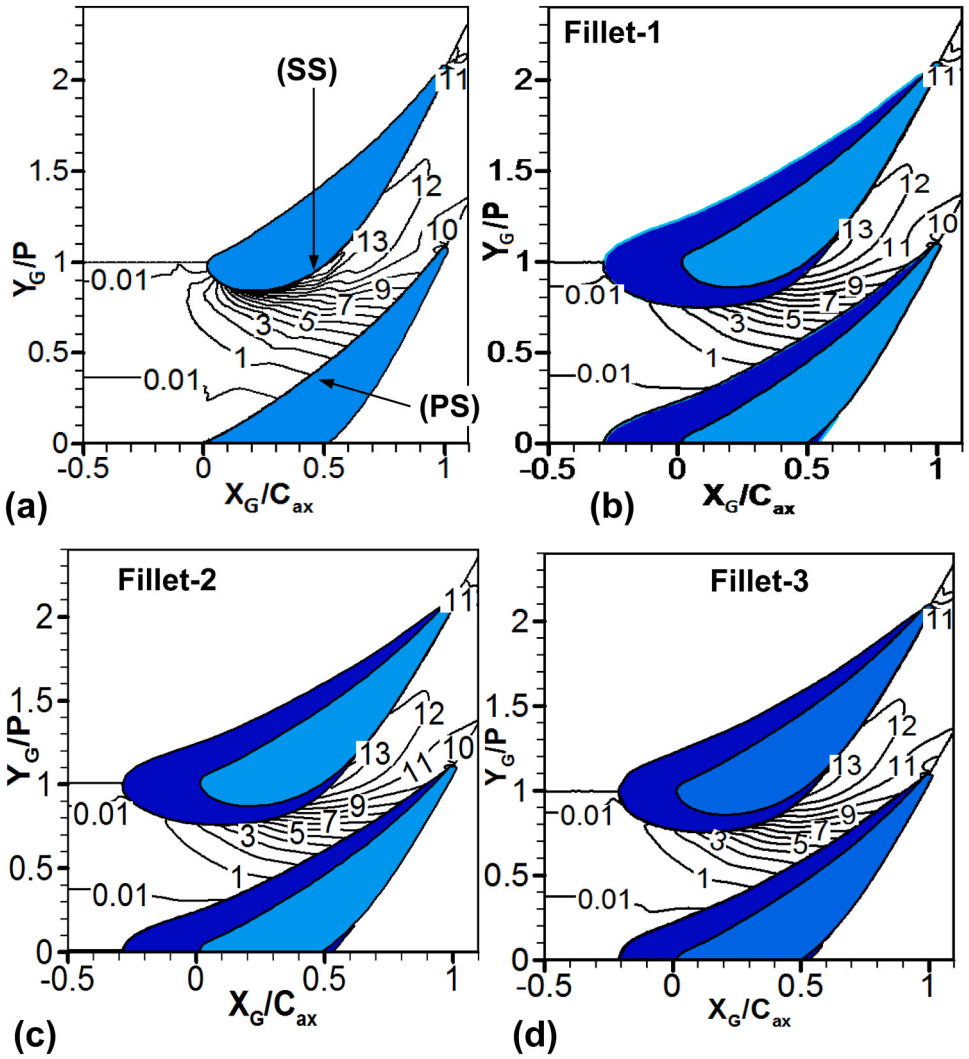


**Fig. 5.** Endwall pressure coefficients, $C_{p,static}$ from computations: (a) Fillet-1, (b) Fillet-2, and (c) Fillet-3.

blade (Baseline 1) or fillet (in Fillet-1, −2, and −3) at a constant axial location ($X_G/C_{ax}$) is computed from the endwall $C_{p,static}$ distributions to get the $C_{p,static}$ at that $X_G/C_{ax}$ location in Fig. 6. The $C_{p,static}$ values at the edge of the Fillet-1 locations or blade profile locations (where the fillet profile is lacking on SS) on the baseline endwall are computed for Baseline 2. The calculated $C_{p,static}$ distributions for Baseline 1 are substantially greater than for the three fillets in ($X_G/C_{ax}$) 0.55 upstream of the suction-side throat area, as shown in Fig. 6. The $C_{p,static}$ distributions for Baseline 2 and fillets, on the other hand, are nearly identical. Because the passage vortices are positioned towards the endwall upstream of the

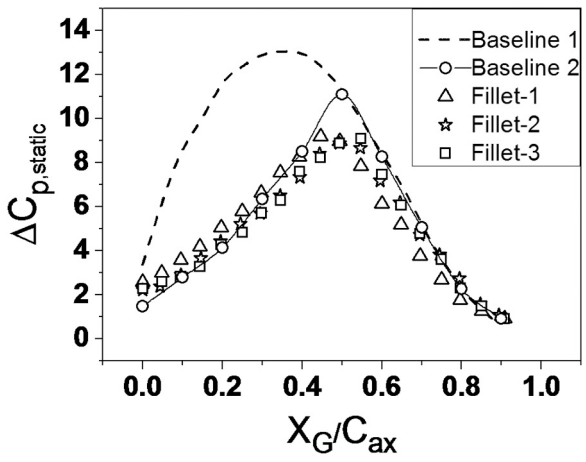


**Fig. 6.** Differences of endwall pressure coefficients, $\Delta C_{p,static}$ (computations) between PS and SS along the endwall ($Z_G/S = 0$).

throat [4,6], their impacts on endwall heat transfer and film cooling are stronger in this area. The fillets efficiently lower the pressure differential between the pressure side and the suction side at the endwall, decreasing a key possibility for the production of a passage vortex. In Fig. 6, the alterations in $C_{p,static}$ contours between fillets are negligible. Because the pressure distributions on the blade profile are the same for the baseline and fillets, the distributions of pitchwise pressure differences for the baseline and fillets increase closer to the near the mid-span, as anticipated.

*Endwall streamlines and yaw angles (computations)*

Figs. 7 and 8 show the streamlines and flow yaw angles obtained from the computations in a plane parallel to the endwall at $Z_G/S = 0.002$. The data of the baseline and three fillets are compared. Fig. 7(b) shows the placement of the blade and fillet in the plane.

The emergence of pressure side-leg and suction side-leg vortices when the streamlines move towards the SS is shown in the baseline case in Fig. 7(a). The apparent positions of boundary layer separation and reattachment lines created based on the concentration and origin of the streamlines in the $Z_G/S = 0.002$ plane are shown in the insert of Fig. 7 (a). Many streamlines appear to begin in the region bordered by the

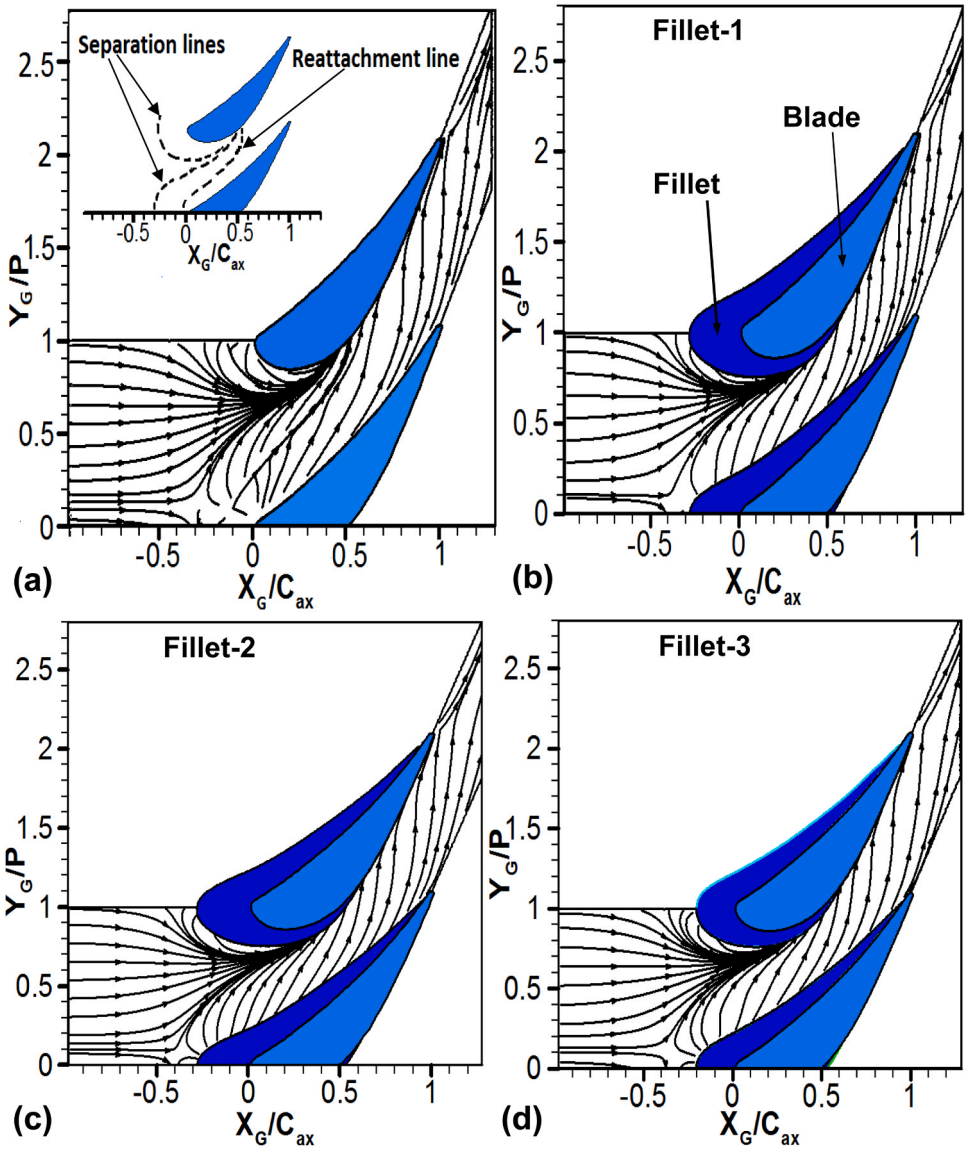


**Fig. 7.** Streamlines (computations) in $Z_G/S = 0.002$ plane: (a) Baseline, (b) Fillet-1, (c) Fillet-2, and (d) Fillet-3.

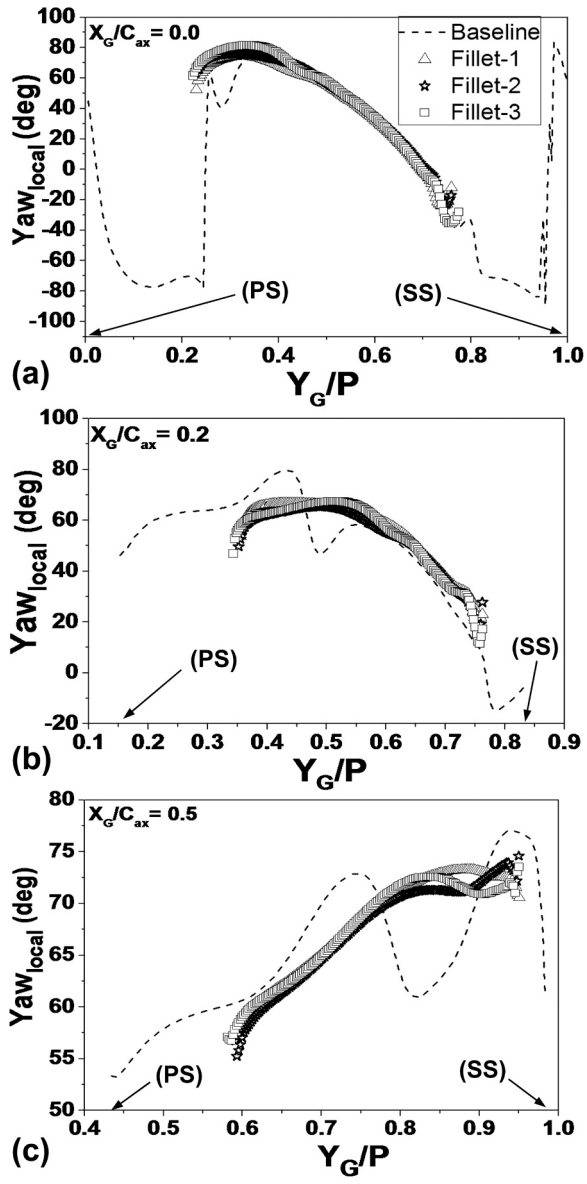


**Fig. 8.** Flow yaw angles (deg) in $Z_G/S = 0.002$ plane at constant axial locations from computations: (a) $X_G/C_{ax} = 0.0$, (b) $X_G/C_{ax} = 0.2$, and (c) $X_G/C_{ax} = 0.5$. Legends are given in 8(a).

separation and reattachment lines, as seen in Fig. 7(a). At $Z_G/S = 0.002$, the suction side-leg vortices and pressure side-leg vortices entice these streamlines from other planes to this plane. As a result, the upstream sections of these streamlines are hidden in Fig. 7. (a). The region of separation and reattachment lines is not readily discernible between the continuous streamlines in the fillet cases in Figs. 7(b) - 7(d). This is because the fillet weakens the vortex legs structure. The streamline trajectories in Figs. 7(b) - 7(d) show little variation across the fillet cases. Because the fillet-effects on the pitchwise pressure differential are confined extremely close to the endwall, the streamlines in other parallel planes (not shown for brevity) further above the endwall are fairly comparable for both the baseline and fillets.

The streamline turnings are depicted in Fig. 8 by the flow yaw angles, which are computed from the local streamwise (X) and pitchwise (Y) velocity components. At three axial positions, the yaw angles are depicted along the pitch-lines. Fig. 1(b) depicts the positive and negative senses of yaw angles. The yaw angles for the three fillets in Figs. 8(a) - 8 (c) are missing at some pitchwise, $Y_G/P$ locations due to the fillet presence. In the displays, the global coordinate $Y_G$ is used to connect the data from Fig. 7 and Fig. 8. The pitch-line measurements in Fig. 8(a) at $X_G/C_{ax} = 0$ are at the passage inlet. The baseline yaw angles in Fig. 8(a) between $0.2 < Y_G/P < 0.5$ are different from the fillet data because they lie inside the big separation zone. The baseline yaw angles within the flow separation and at the flow reattachment are also different from the fillet data, with $0.3 < Y_G/P < 0.6$ along $X_G/C_{ax} = 0.2$ of Fig. 8(b) and $0.65 < Y_G/P < 0.97$ along $X_G/C_{ax} = 0.5$ of Fig. 8(c). In comparison to the fillets, the fluctuations in yaw angles inside the separation and towards the reattachment in Figs. 8(a) - 8(c) are significant for the baseline. In Figs. 8(a) - 8(c), the distributions of local yaw angles are almost the same for all fillets and progressively rise or decrease from PS to SS. As a result, the fillets provide advantageous streamline distributions towards the endwall for film cooling location and orientation. Fig. 9 illustrates the difference in mass-averaged yaw angles of streamlines, $(\Delta Yaw)_{mass\text{-}av}$ in Plane-1 and −2 in the Z/S direction. The pitchwise mass-averaged yaw angle at a specific Z/S position and at the plane's mid-span location are employed in Eq. (13). Because of the strong streamline turnings in the boundary layer and passage vortex, the values of $(\Delta Yaw)_{mass\text{-}av}$ in both planes in Fig. 9 are considerably large at $Z/S < 0.2$ at the endwall. The baseline and fillets have similar distributions of $(\Delta Yaw)_{mass\text{-}av}$ along the span in Fig. 9(a). However, the baseline $(\Delta Yaw)_{mass\text{-}av}$ in Fig. 9(b) at $Z/S < 0.04$ is roughly 2° higher than the fillets.

$$(\Delta Yaw)_{mass-av} = Yaw_{mass-av} - \left(Yaw_{midspan}\right)_{mass-av} \tag{13}$$

The stagnation plane touches the blade leading-edge (LE) and is parallel to the axial $X_G$ direction, which is where the streamlines at the endwall of Fig. 10 are presented. In the figure, the LE is at $X_G/C_{ax} = 0$. The three fillets at the leading-edge are identified by the void triangular sections in Figs. 10(b) - 10(d). The LE horseshoe vortex, which is the origin of the vortex legs in the passage, is identified by rolling up the streamlines right above the endwall ($Z_G/S = 0$) for the baseline and fillet

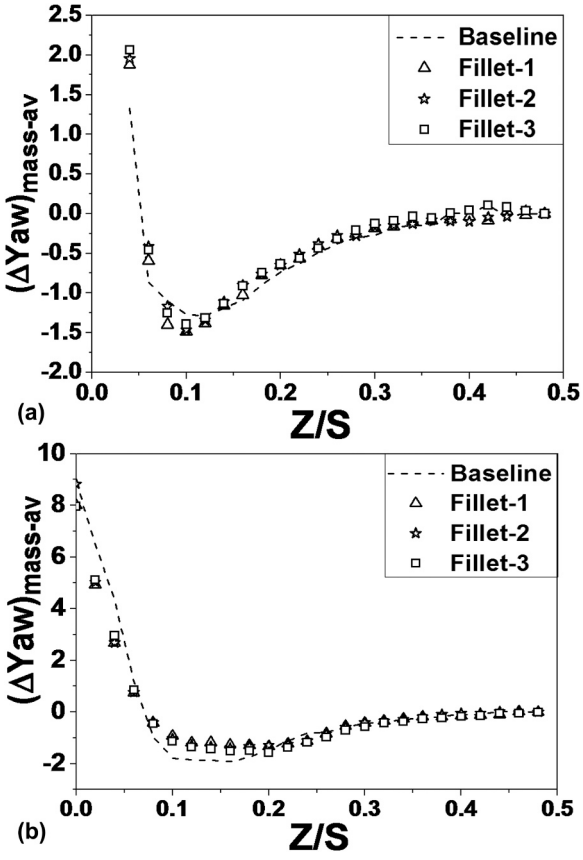


**Fig. 9.** Difference of mass-averaged Yaw angles, $(\Delta Yaw)_{mass\text{-}av}$ (deg) from computations in: (a) Plane-1, and (b) in Plane-2.

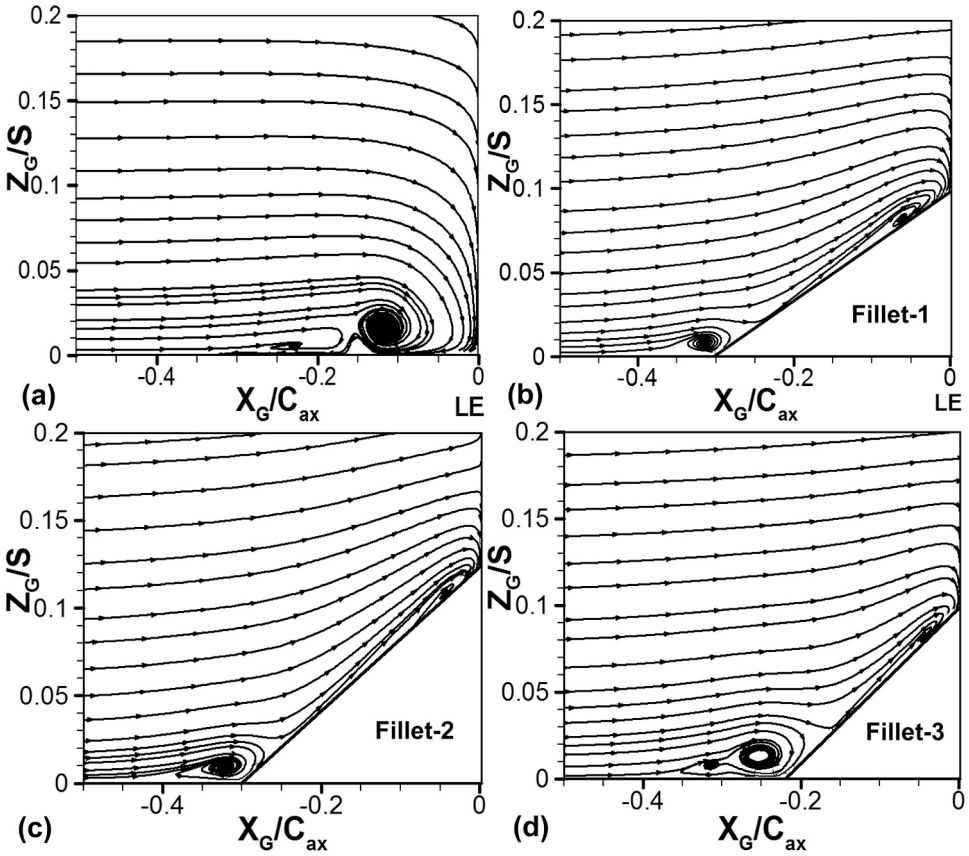


**Fig. 10.** Streamlines (computations) at Stagnation plane: (a) Baseline, (b) Fillet-1, (c) Fillet-2 and (d) Fillet-3.

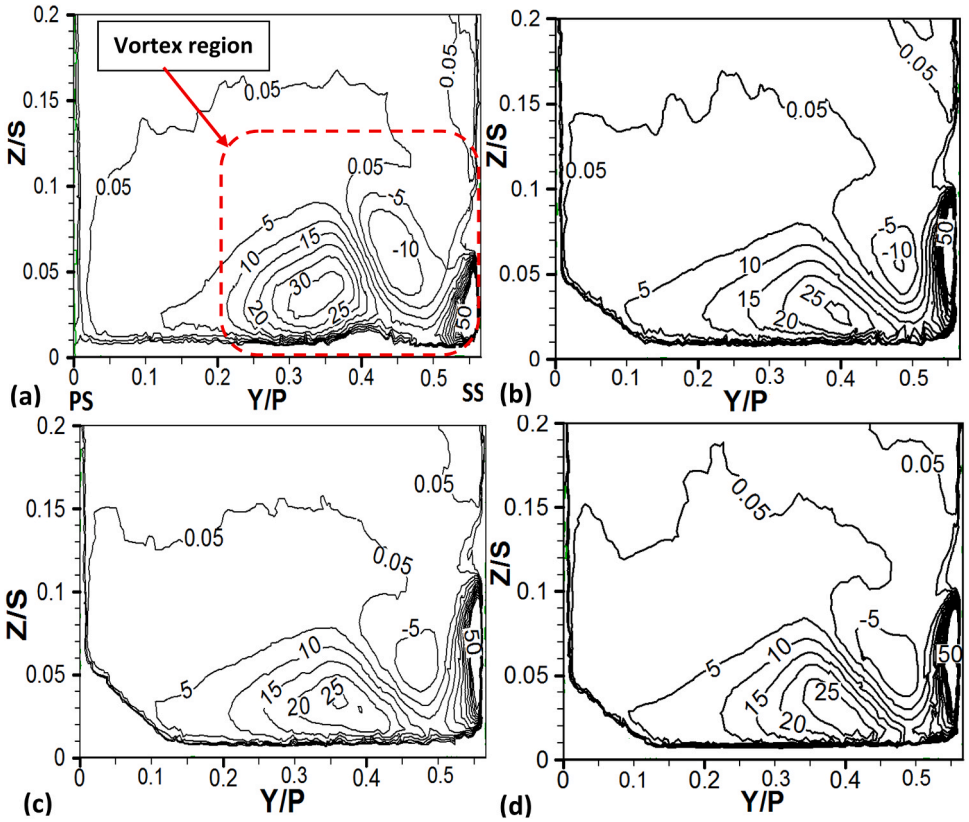


**Fig. 11.** Normalized axial vorticity contours (computations) in Plane-1 at $X_G/C_{ax} = 0.58$: (a) Baseline, (b) Fillet-1, (c) Fillet-2 and (d) Fillet-3.

cases in Figs. 10(a) - 10(d). The baseline horseshoe vortex is roughly twice the size of the fillet vortex. Fillets diminish the thickness of the incoming boundary layer in the stagnation plane, and therefore the horseshoe vortex [10,15]. In Fig. 10(d), the horseshoe vortex for Fillet-3 appears to be significantly bigger than the other two fillets. In the filleted route, the smaller LE vortex formations weaken and diminish the passage vortex.

*Axial vorticity (computations)*

The contours of normalised axial vorticity ($\omega_x$C/U) computed between the baseline and fillets in Plane-1 and −2, respectively, are shown in Figs. 11 and 12. The figures' axes correspond to the local coordinate systems shown in Fig. 1(b). In Figs. 11 and 12, the positive contour values imply axial vorticity ($\omega_x$) in the '+x' direction, and the vortex rotates counter-clockwise. The intense vortical movements or the orientation of the core of the passage vortex toward the x-direction, or both, create the large magnitudes of $\omega_x$C/U. The vortex induces mixing between the endwall and freestream area fluids, which increases local convective heat transfer and secondary losses while diminishing the efficiency of film cooling [6,27]. The vortex, or swirling motion of fluid, occurs at the junction where the endwall (the boundary of the flow passage) meets the freestream area (the undisturbed flow away from surfaces) as shown in Figs. 11 and 12. This swirling motion causes mixing between these fluid regions, leading to intensified convective heat transfer in the local vicinity. However, this increased mixing also results in secondary losses, which represent additional energy dissipation beyond the primary function of the system. As shown in Fig. 7(a), the origin of the vortex starts from the flow separation line, upstream of the leading edge to the trailing edge.

In Plane-1 of Fig. 11, the blade's pressure and suction sides are on the left and right sides of the plots, respectively. In Figs. 11(b) - 11(d), the triangular filleted portions in the lower left corner do not include any data. The interactions of the pressure side-leg vortices and suction side-leg vortices in Figs. 11(a) - 11(d) generate the positive and negative contours of $\omega_x$C/U defined by Z/S < 0.1 and Y/P > 0.2. Because the fillet weakens the vortex structures, the contour magnitudes and size of this high vorticity zone are less for the fillets than for the baseline. The vorticity of the vortex-leg cores in Fillet-1 and −2 of Figs. 11(b) - 11(c) in 0.3 < Y/P < 0.5 are similarly, marginally less than those in Fillet-3. The filleted passage reduces the LE vortex and pitchwise pressure gradient near the endwall as shown previously to weaken the passage-vortex legs. The filleted passage is then expected to reduce the endwall heat transfer and increase the endwall film-cooling effectiveness. The values of ($\omega_x C/U$) ≥ 50 in Fig. 11 are triggered by the interactions between the passage vortex legs and blade-surface boundary layer.

The passage vortex core as the flow departs the cascade causes the elevated values of $\omega_x$C/U on the right side of Figs. 12(a) - 12(d). Just upstream of Y/P = 0 and 1, the blade trailing edge (TE) is present. The passage vortex is situated above the endwall area in Plane-2, based on the high contour magnitudes in Fig. 12. The feeble and smaller passage vortex in the filleted passage is shown by the lower values and area of $\omega_x$C/U in the vortex-core for the fillets of Figs. 12(b) - 12(d) than for the baseline. However, the contour distributions in Figs. 12(b) - 12(d) are nearly identical, indicating that the fillet geometries have little influence.

*Total pressure loss coefficient for the computation, $C_{pt,loss}$*

The total pressure loss across the cascade reflects the consequences of

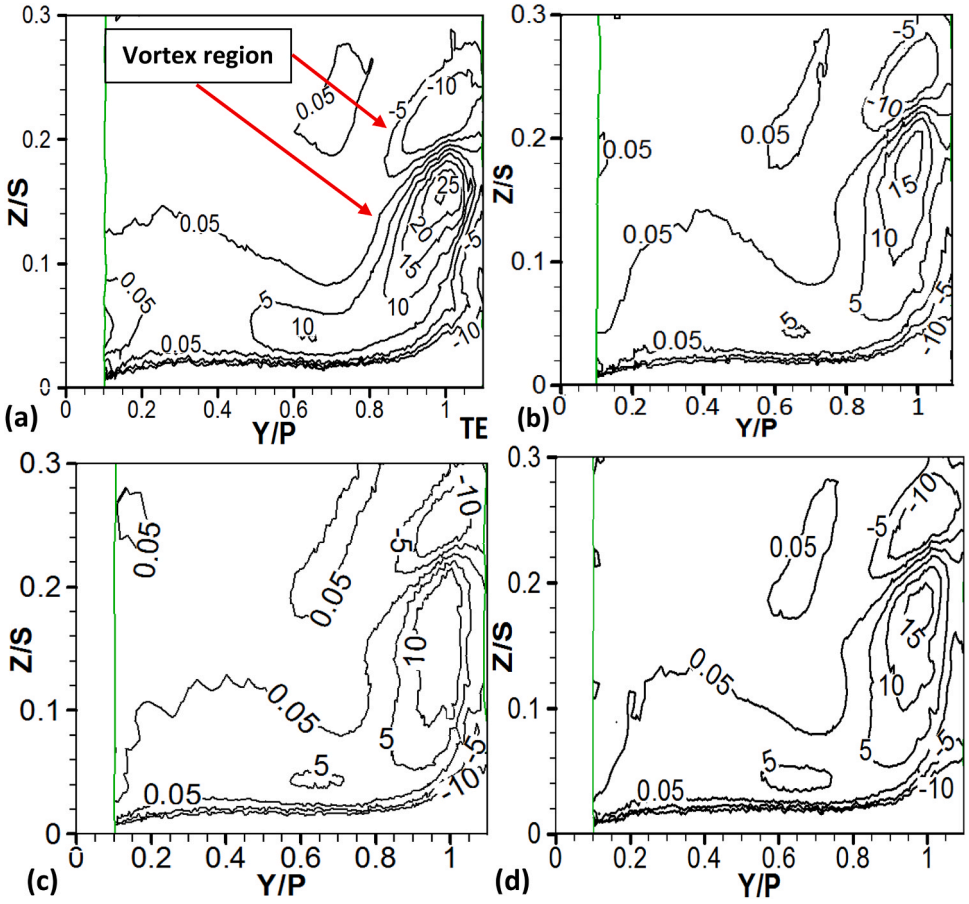


**Fig. 12.** Normalized axial vorticity contours (computations) in Plane-2 at $X_G/C_{ax}$ = 1.04: (a) Baseline, (b) Fillet-1, (c) Fillet-2, and (d) Fillet-3.

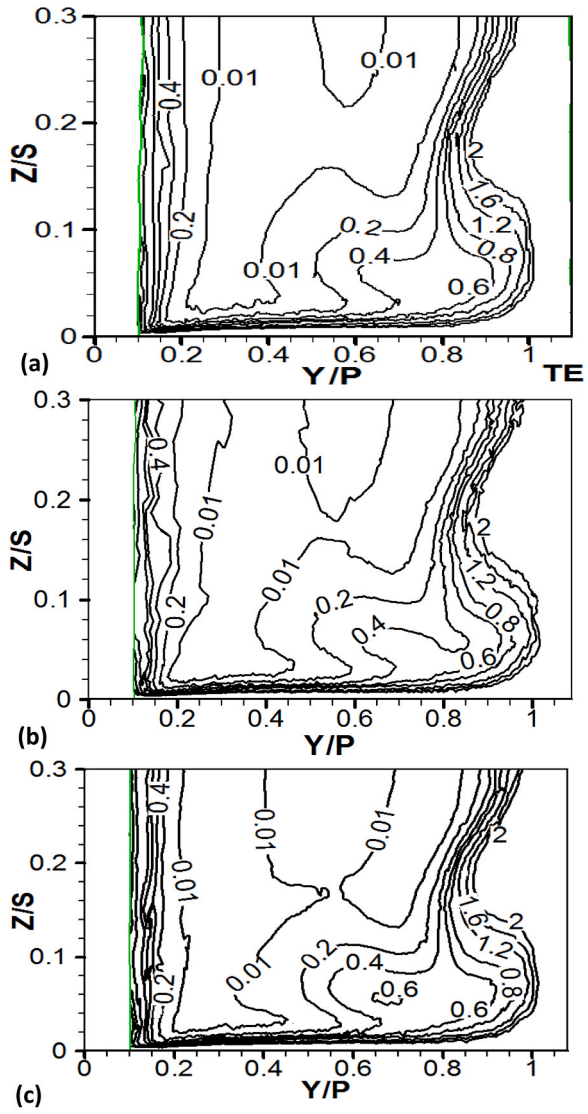


**Fig. 13.** Total pressure loss coefficient, $C_{pt,loss}$ contours (computations) in Plane-2 at $X_G/C_{ax} = 1.04$: (a) Fillet-1, (b) Fillet-2 and (c) Fillet-3.

the decreased passage vortex in the filleted passage. The total pressure loss coefficients ($C_{pt,loss}$) in Plane-2, computed for the three filleted passageways are shown in Fig. 13. The secondary flow diminution at the cascade outlet are indicated by the $C_{pt,loss}$, which is calculated from the local total pressure distributions, $P_{t,x,}$ in Eq. (12). The total pressure loss and secondary losses in the blade path way increase as the $C_{pt,loss}$ increases, as does the passage vortex. Fig. 13 shows the fillet data, which may be compared to the baseline computational findings in Fig. 4. (b). The elevated values of $C_{pt,loss}$ at $Y/P > 0.5$ in Figs. 13(a) - 13(c) are due to the passing vortex near the cascade outlet, as previously stated. The TE wake and passage vortex interactions with the TE wake result in the higher contours at $Y/P < 0.25$ and $Y/P > 0.9$. When the computing case in Fig. 4(b) is compared to the data in Fig. 13, the fillet lowers the region of $C_{pt,loss} \geq 0.4$ at the lower right side of Figs. 13(a) - 13 (c). Also, for the Fillet-2, the contour region of $C_{pt,loss} \geq 0.4$ around the lower right corner appears to be the smallest. According to the overall mass-averaged $(C_{pt,loss})_{mass\text{-}av}$ in Plane-2 reported in Table 3 and calculated using Eq. (10) the fillets lower the loss coefficients by 8–11 percent juxtaposed to the baseline computational findings. The Fillet 2 has the lowest overall $(C_{pt,loss})_{mass\text{-}av}$. Because the measurement errors in the TE vortex area are considerable, the difference in baseline $(C_{pt,loss})_{mass\text{-}av}$ between the experiment and calculations in Table 3 is significant.

**Table 3**
Overall mass-averaged of total pressure loss coefficients in Plane-2.

| | Overall $(C_{pt,\ loss})_{mass\text{-}av}$ |
|---|---|
| Experiment, Baseline | 0.870 |
| Computation, Baseline | 0.70 |
| Computation, Fillet-1 | 0.634 |
| Computation, Fillet-2 | 0.624 |
| Computation, Fillet-3 | 0.643 |

## Summary and conclusion

In a low-speed vane cascade with a broad fillet at the blade-endwall junction, computational predictions of the endwall region flow-field are provided. The goals are to look into the effects of fillet shape variations on the endwall secondary flows and overall pressure losses. The fillet is not designed to compensate for flow losses. The 2-D cascade model is based on the contour of the GE-E$^3$ engine's nozzle guiding vane. To mimic manufacturing error in the fillet employment, three geometric variants of a fillet profile are examined. The fillets are used betwixt the blade leading edge and the path way throat area, although their height and endwall width are distinct from one another. The experimental data in a cascade of the same shape as in the computations validates the computational model for the baseline (without fillet). For the cascade incident flow Reynolds number of $2.01 \times 10^5$, the results are shown here.

- The results show that when fillets are used, the static pressure distributions along the passage endwall remain unchanged.
- The pitchwise pressure gradient on the route endwall from the pressure to suction side is, however, less for the fillets than for the baseline upstream of the throat area. The fillets also minimize the horseshoe-vortex structure on the leading edge, which influences the passage vortex.
- When fillets are used, the endwall flow separation zone between the separation line and the reattachment line is greatly decreased, weakening the passage vortex. The fillets then progressively alter the flow yaw angles towards the endwall from pressure to suction, which can help with endwall film coverage. In comparison to the fillets, the changes in flow yaw angles towards the endwall for the baseline are substantially bigger, especially in the separation zone. However, the effects of fillet geometric differences on streamlines and yaw angles in the endwall area are negligible.
- The results also reveal that as the size and strength of the passage vortex is reduced, the axial vorticity along the filleted channel decreases, indicating less turbulent flow mixing in the endwall area.
- The axial vorticity, on the other hand, is unaffected by the fillet changes. The fillets' total pressure losses along the cascade channel are thus lower than the baseline. However, the losses do not differ much across the fillets. Simple modifications in the specified fillet shape during production, according to the current research, are unlikely to have a major impact on the fillet's advantages.

## Statement of unavailability of data

The raw data supporting the findings presented in this article is currently unavailable for public access. Several factors have contributed to the unavailability of the data, including confidentiality, limitations imposed by third-party data providers.

The nature of the data used in this study, as well as legal and ethical constraints, prevents us from providing public access to the dataset at this time. We recognize the importance of data transparency and reproducibility in scientific research. Besides, all the data needed for reproducibility are already given in the manuscript.

## Declaration of Competing Interest

I declared that there is no conflict of interest as regards the manuscript submitted. This is in accordance with the ethics of publishing at the Journal of Engineering Research.

## Acknowledgment

The authors are indeed indebted for the fiscal support of AMRSCOR program of South Africa. The help of Mr. K. Arnachellan in the experiments is equally appreciated.

## References

[1] A.S. Shote, G.I. Mahmood, J.P. Meyer, Endwall adiabatic film-cooling effectiveness with upstream film cooling schemes in a filleted vane cascade, Proc. 14th Int. Conf. Heat Transf., Fluid Mech. Thermodyn. (HEFAT) (2019) 510–523.
[2] Y. Shi, J. Li, Z. Feng, Influence of rotor blade fillets on aerodynamic performance of turbine stage, Proc. ASME Turbo Expo. (2010) 1657–1668.
[3] A.S. Shote, G.I. Mahmood, J.P. Meyer, Influences of large fillets on endwall flows in a vane cascade with upstream slot film-cooling, Exp. Therm. Fluid Sci. 112 (2020) 109951.
[4] M.B. Kang, K.A. Thole, Flowfield measurements in the endwall region of a stator vane, J. Turbomach. 122 (3) (2000) 458–466.
[5] Hermanson, K., Kern, S., Picker, G., and Parneix, S., 2003, Predictions of External Heat Transfer for Turbine Vanes and Blades With Secondary Flowfields, Journal of Turbomachinery, 125(1), pp. 107-113.
[6] Acharya, S., and Mahmood, G.I., 2007, 3-D Aerodynamics, The Gas Turbine Handbook, National Energy Technology Laboratory (NETL)-DOE, 1.0, Chap. 4.3, USA.
[7] A.K. Saha, S. Acharya, Computations of turbulent flow and heat transfer through a three-dimensional nonaxisymmetric blade passage, J. Turbomach. 130 (3) (2008), pp. 031008-031008-031010.
[8] D. Torre, R. Vázquez, E. d l R. Blanco, H.P. Hodson, A new alternative for reduction in secondary flows in low pressure turbines, ASME J. Turbomach. 133 (1) (2011), 011029(011021)-011029(011010).
[9] P. Ligrani, G. Potts, A. Fatemi, Endwall aerodynamic losses from turbine components within gas turbine engines, Propuls. Power Res. 6 (1) (2017) 1–14.
[10] G.A. Zess, K.A. Thole, Computational design and experimental evaluation of using a leading edge fillet on a Gas Turbine Vane, J. Turbomach. 124 (2) (2002) 167–175.
[11] S. Becz, M.S. Majewski, L.S. Langston, Leading edge modification effects on turbine cascade endwall loss, Proc. ASME Turbo Expo. (2003) 359–367.
[12] T.I.P. Shih, Y.L. Lin, Controlling secondary-flow structure by leading-edge airfoil fillet and inlet swirl to reduce aerodynamic loss and surface heat transfer, J. Turbomach. 125 (1) (2003) 48–56.
[13] S. Becz, M.S. Majewski, L.S. Langston, An experimental investigation of contoured leading edges for secondary flow loss reduction, Proc. ASME Turbo Expo., ASME (2004) 1407–1415.
[14] M.W. Benner, S.A. Sjolander, S.H. Moustapha, The influence of leading edge geometry on secondary losses in a turbine cascade at the design incidence, ASME J. Turbomach. 126 (2) (2004) 277–287.
[15] G.I. Mahmood, R. Gustafson, S. Acharya, Experimental investigation of flow structure and nusselt number in a low-speed linear blade passage with and without leading-edge fillets, J. Heat. Transf. 127 (2005) 499–512.
[16] R. Saha, J. Fridh, T. Fransson, B.I. Mamaev, M. Annerfeldt, Experimental studies of leading edge contouring influence on secondary losses in transonic turbines, Proc. ASME Turbo Expo. (2012) 1109–1119.
[17] R. Saha, B.I. Mamaev, J. Fridh, B. Laumert, T.H. Fransson, Influence of prehistory and leading edge contouring on aero performance of a three-dimensional Nozzle Guide Vane, J. Turbomach. 136 (7) (2014), 071014-071014-071010.
[18] Z.J. Wei, W.Y. Qiao, J. Liu, W.H. Duan, Reduction of endwall secondary flow losses with leading-edge fillet in a highly loaded low-pressure turbine, Proc. Inst. Mech. Eng., Part A, J. Power Energy 230 (2) (2016) 184–195.
[19] H. Sauer, R. Muller, K. Vogeler, Reduction of secondary flow losses in turbine cascades by leading edge modifications at the endwall, ASME J. Turbomach. 123 (2) (2001) 207–213.
[20] S. Mank, L. Duerrwaechter, M. Hilfer, R. Williams, S. Hogg, G. Ingram, Secondary flows and fillet radii in a linear turbine cascade, Proc. ASME Turbo Expo. (2014). V02CT38A011.
[21] B.I. Mamaev, R. Saha, J. Fridh, The influence of a special fillet between the endwall and airfoil at the leading edge on the performance of the turbine nozzle diaphragm, Therm. Eng. 60 (3) (2013) 217–222.
[22] L.P. Timko, Contract Report for NASA, Energy Effic. Engine High. Press. Turbine Compon. Test. Perform. Rep. (1990).
[23] T.G. Beckwith, R.D. Marangoni, J.H. Lienhard, Mechanical Measurements, Pearson Prentice Hall, , USA, 2007.
[24] CD-adapco, 2013, STAR-CCM+ User Guide Version 8.06, Melville, New York, USA.
[25] S. Winkler, E. Kerber, T. Hitz, B. Weigand, P. Ligrani, Numerical second law analysis around a turbine guide vane using a two-equation turbulence model and comparison with experiments, Int. J. Therm. Sci. 116 (Supplement C) (2017) 91–102.
[26] T. Jimbo, D. Biswas, Y. Niizeki, Studies on unsteady flow characteristics in a high pressure turbine cascade based on a high-order large eddy simulation turbulence model, J. Turbomach. 134 (5) (2012), 051018-051018-051019.
[27] A.K. Saha, G.I. Mahmood, S. Acharya, The role of leading-edge contouring on endwall flow and heat transfer: computations and experiments, Proc. ASME Turbo Expo., ASME (2006) 1105–1118.